

Article

# Highly Sensitive NO<sub>2</sub> Gas Sensors Based on MoS<sub>2</sub>@MoO<sub>3</sub> Magnetic Heterostructure

Wei Li <sup>1,2</sup>, Mahboobeh Shahbazi <sup>1</sup>, Kaijian Xing <sup>3</sup>, Tuquabo Tesfamichael <sup>2,4,\*</sup>, Nunzio Motta <sup>1,2,\*</sup> and Dong-Chen Qi <sup>1,2,\*</sup> 

<sup>1</sup> School of Chemistry and Physics, Queensland University of Technology, Brisbane, QLD 4001, Australia; w73.li@hdr.qut.edu.au (W.L.); mahboobeh.shahbazi@qut.edu.au (M.S.)

<sup>2</sup> Centre for Materials Science, Queensland University of Technology, Brisbane, QLD 4001, Australia

<sup>3</sup> School of Physics and Astronomy, Monash University, Clayton, VIC 3800, Australia; kaijian.xing@monash.edu

<sup>4</sup> School of Mechanical, Medical and Process Engineering, Queensland University of Technology, Brisbane, QLD 4001, Australia

\* Correspondence: t.tesfamichael@qut.edu.au (T.T.); n.motta@qut.edu.au (N.M.); dongchen.qi@qut.edu.au (D.-C.Q.)

**Abstract:** Recently, two-dimensional (2D) materials and their heterostructures have attracted considerable attention in gas sensing applications. In this work, we synthesized 2D MoS<sub>2</sub>@MoO<sub>3</sub> heterostructures through post-sulfurization of α-MoO<sub>3</sub> nanoribbons grown via vapor phase transport (VPT) and demonstrated highly sensitive NO<sub>2</sub> gas sensors based on the hybrid heterostructures. The morphological, structural, and compositional properties of the MoS<sub>2</sub>@MoO<sub>3</sub> hybrids were studied by a combination of advanced characterization techniques revealing a core-shell structure with the coexistence of 2H-MoS<sub>2</sub> multilayers and intermediate molybdenum oxysulfides on the surface of α-MoO<sub>3</sub>. The MoS<sub>2</sub>@MoO<sub>3</sub> hybrids also exhibit room-temperature ferromagnetism, revealed by vibrating sample magnetometry (VSM), as a result of the sulfurization process. The MoS<sub>2</sub>@MoO<sub>3</sub> gas sensors display a *p*-type-like response towards NO<sub>2</sub> with a detection limit of 0.15 ppm at a working temperature of 125 °C, as well as superb selectivity and reversibility. This *p*-type-like sensing behavior is attributed to the heterointerface of MoS<sub>2</sub>-MoO<sub>3</sub> where interfacial charge transfer leads to a *p*-type inversion layer in MoS<sub>2</sub>, and is enhanced by magnetic dipole interactions between the paramagnetic NO<sub>2</sub> and the ferromagnetic sensing layer. Our study demonstrates the promising application of 2D molybdenum hybrid compounds in gas sensing applications with a unique combination of electronic and magnetic properties.

**Keywords:** heterostructure; 2D materials; sulfurization; nitrogen dioxide; gas sensor; molybdenum trioxide; molybdenum disulfides



**Citation:** Li, W.; Shahbazi, M.; Xing, K.; Tesfamichael, T.; Motta, N.; Qi, D.-C. Highly Sensitive NO<sub>2</sub> Gas Sensors Based on MoS<sub>2</sub>@MoO<sub>3</sub> Magnetic Heterostructure. *Nanomaterials* **2022**, *12*, 1303. <https://doi.org/10.3390/nano12081303>

Academic Editors: Andres Castellanos-Gomez and Sergei Kulinich

Received: 9 February 2022

Accepted: 8 April 2022

Published: 11 April 2022

**Publisher's Note:** MDPI stays neutral with regard to jurisdictional claims in published maps and institutional affiliations.



**Copyright:** © 2022 by the authors. Licensee MDPI, Basel, Switzerland. This article is an open access article distributed under the terms and conditions of the Creative Commons Attribution (CC BY) license (<https://creativecommons.org/licenses/by/4.0/>).

## 1. Introduction

The rapid development in technologies and industrial activities in recent decades has brought unprecedented convenience to our life. However, it has also led to a rapid increase in the emission of toxic and greenhouse gases bringing harm to our planet and human health [1,2]. Toxic gases, such as CO, NO<sub>2</sub>, SO<sub>2</sub>, NO, NH<sub>3</sub>, etc., inflict respiratory damage on humans, such as lung cancers, cough, and asthma, even at an extremely low concentration [2]. Among them, NO<sub>2</sub> acting as a typical toxic gas has received particular attention in the last decades. NO<sub>2</sub> not only produces acid rain harming the environment but is also a major contributor to severe respiratory symptoms when its concentration is higher than 1 ppm [3–6]. As a consequence, it is crucially necessary to develop highly selective, sensitive, rapid response, and low-cost sensors for detecting and monitoring trace amounts of NO<sub>2</sub> [7].

To meet this challenge, numerous semiconducting materials have been extensively studied to develop conductometric gas sensors which are capable of detecting a wide range

of analytical gases [8], such as metal oxide semiconductors, conducting polymers, carbon nanotubes, and metal dichalcogenide semiconductors. Among these sensitive materials, metal oxides semiconductors (MOSs) have attracted the most attention for utilization in the preparation of gas sensors due to their simple structure, high sensitivity, chemical stability, and low cost. Particularly, MOSs have been developed in great numbers of nanostructures with different dimensions, such as one-dimensional (1D) nanoribbon, nanowire, nanorod, two-dimensional (2D) nanosheet, nanoplate, nanoflake, and three-dimensional (3D) nanoflower, the nanoarray [5,7]. The nanostructured MOSs have a high surface-to-volume ratio which supports more adsorption sites for analyte gas molecules to enhance the gas sensing behavior. However, the high working temperature, low selectivity, and high power consumption also impede their wider and more versatile applications [9,10].

Recently, two-dimensional (2D) materials have emerged as a new materials platform enabling breakthroughs in fundamental research and transformative technologies [11,12]. The absence of surface dangling bonds and unique atomic-level uniformity make them very appealing for developing a plethora of optical, electronic, and energy applications. 2D materials also have intrinsic high surface-to-volume ratio providing abundant adsorption sites, as well as enhanced electronic properties due to carrier confinement. These distinct attributes make 2D materials particularly attractive for gas sensing applications [7,13–15]. Indeed, gas sensors based on typical 2D materials including graphene, MXenes, transition metal dichalcogenides (TMDCs), and phosphorene have been widely demonstrated [15–17]. In particular, MoS<sub>2</sub>, predicated theoretically as one of the most prominent candidates for 2D material-based gas sensors [18,19], has yielded a promising sensing performance to NO<sub>2</sub> albeit while still presenting challenges, such as low sensitivity and unsatisfactory selectivity [20], which limit practical applications [20,21].

On the other hand, layered metal oxides have also emerged as a new class of van der Waals 2D materials [22]. With the combination of the desirable properties of both oxide materials and 2D materials, they exhibit great potential in numerous fields, such as gas sensing, electronics, optics, catalysis, and energy storage [23–27]. The thermodynamically stable  $\alpha$ -MoO<sub>3</sub> is a typical 2D oxide with a layered crystal structure and has received a lot of attention recently for building novel electronic and optoelectronic devices [28]. It has also been demonstrated for various gas sensing applications [29,30], including achieving ultrahigh sensitivity and superior selectivity to NO<sub>2</sub> [27,31]. Driven by the prominent prospect of 2D van der Waals heterostructures with rationally tailored properties [32,33], enormous efforts have also been devoted to the synthesis and study of hybrid compounds of MoS<sub>2</sub>@MoO<sub>3</sub>. For instance, electrocatalysts based on MoO<sub>3</sub>@MoS<sub>2</sub> nanosheets were reported to enhance hydrogen evolution reaction [24,34–36], and MoO<sub>3</sub>@MoS<sub>2</sub> nanowires were also reported as anodes in lithium-ion batteries [37]. There has also been increasing interest in MoS<sub>2</sub>@MoO<sub>3</sub> composites in gas sensing. Singh et al. synthesized MoS<sub>2</sub>@MoO<sub>3</sub> nanocomposites with the hydrothermal method for NH<sub>3</sub> sensing in a humid environment [38]; Li et al. showed an enhanced CO gas sensor based on MoS<sub>2</sub>@MoO<sub>3-x</sub> nanosheets synthesized via the solvothermal method [39]. However, NO<sub>2</sub> gas sensors based on MoS<sub>2</sub>@MoO<sub>3</sub> heterostructure remain largely unexplored.

In this work, we developed a highly sensitive NO<sub>2</sub> sensor based on MoS<sub>2</sub>@MoO<sub>3</sub> nanoribbons by a post-sulfurization method. The morphology and structures of the as-synthesized MoS<sub>2</sub>@MoO<sub>3</sub> hybrid heterostructures were characterized by field-emission scanning electron microscopy (FE-SEM), and transmission electron microscopy (TEM). The structural, compositional, and magnetic properties of the MoS<sub>2</sub>@MoO<sub>3</sub> hybrids were fully investigated by X-ray diffraction (XRD), Raman spectroscopy, X-ray photoelectron spectroscopy (XPS), and magnetic measurement. The MoS<sub>2</sub>@MoO<sub>3</sub> nanoribbons-based gas sensor exhibited a *p*-type gas sensing behavior to the analytical gases, with high sensitivity, impressive selectivity, and good reproducibility to NO<sub>2</sub> at an optimal operating temperature of 125 °C.

## 2. Materials and Methods

### 2.1. Synthesis of MoO<sub>3</sub>

Before the deposition of MoO<sub>3</sub> nanoribbons, Au/Ti (100 nm/10 nm) interdigital contact electrodes were deposited on SiO<sub>2</sub> (285 nm)/Si substrates through a shadow mask by using electron-beam physical vapor deposition (E-beam PVD). The interdigital electrodes consist of four pairs of electrodes with a width of 300 μm and a spacing of 200 μm (Figure 1). MoO<sub>3</sub> nanoribbons were then synthesized via vapor phase transport (VPT) directly on the substrates with pre-patterned electrodes, following our previous reported approach (Figure 1) [27]. In brief, 0.125 g MoO<sub>3</sub> (99.95% purity, Strem Chemicals) powder was placed in the center of high-temperature heating Zone I (upstream of the tube) of a dual-zone furnace (LABEC—Split Horizontal Tube Furnace) inside a quartz tube (1000 mm in length, 50 mm in diameter), where the temperature was set to 750 °C (Figure 1). Simultaneously, the SiO<sub>2</sub>/Si substrate was placed in the low-temperature Zone II (downstream of the tube) with a temperature of 600 °C. Synthetic air (hydrocarbon impurities < 0.1 ppm) was used as the carrier gas with an airflow of 120 sccm.

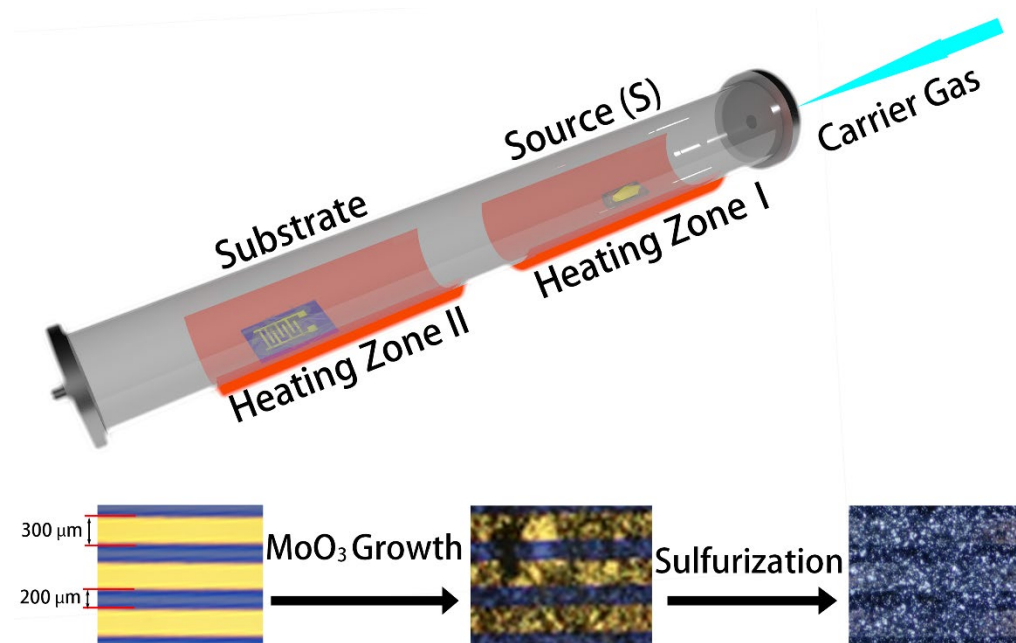


**Figure 1.** Above: schematic illustration of the post-sulfurization process for MoO<sub>3</sub> nanoribbons, the SiO<sub>2</sub>/Si substrate with pre-patterned interdigital electrodes. Below: the optical images of the device before and after MoO<sub>3</sub> synthesis and subsequent sulfurization.

### 2.2. Sulfurization

The subsequent sulfurization of the synthesized MoO<sub>3</sub> nanoribbons on SiO<sub>2</sub>/Si substrates was performed in the same quartz tube by replacing the boat with MoO<sub>3</sub> powder with 0.6 g sulfur powder (99.3% purity, Ajax Finechem, Sidney, NSW, Australia) at a temperature of 280°. Meanwhile, the substrates with MoO<sub>3</sub> nanoribbons were placed in the same location with a temperature of 550°. Pure argon was used as the carrier gas with an airflow of 120 sccm.

### 2.3. Materials Characterizations

A Leica DM6000 optical microscope (Wetzlar, Germany) and Zeiss sigma field emission scanning electron microscope (FESEM, Jena, Germany) were utilized to characterize the surface morphology of the as-grown samples before and after sulfurization. Transmission electron microscopy (TEM) and energy dispersive spectroscopy (EDS) were collected using a JEOL 2100 electron microscope (Tokyo, Japan) to analyze the detailed structure and crystallinity of the as-grown samples after sulfurization. The X-ray diffraction (XRD) pattern

was carried out using PANalytical MPD Cu powder XRD with Cu  $K_{\alpha}$  radiation source (Almelo, Netherlands) to study the phase compositions and crystallographic structures of the as-synthesized samples before and after sulfurization. A Raman microscope (Renishaw inVia, Wotton-under-Edge, UK) with an excitation laser of 532 nm in wavelength was employed to study the structural vibration of the samples both before and after sulfurization. The stoichiometry and electronic structure of as-grown samples after sulfurization were studied by X-ray photoelectron spectroscopy (XPS) with a Kratos AXIS Supra photoelectron spectrometer using a monochromatized Al  $K_{\alpha}$  X-ray source (Manchester, UK). The magnetic property of the sulfurated samples was measured by a vibrating-sample magnetometer (VSM) using a Cryogen-free 5 T system (London, UK).

#### 2.4. Characterization of Gas Sensors

A home-built multichannel gas sensing test system was used to evaluate the gas sensing performance of the fabricated gas sensor, shown in Figure S2. The gas sensor was mounted at the top of the ceramic heater providing an operating temperature for the device controlled by an Agilent E3649 power supply (Santa Clara, CA, USA). The test chamber with an internal volume of 1100 mL was coupled to five high precision mass flow controllers (MFC, MKS 1479A, 200 sccm, Andover, MA, USA) capable of supporting five different analytical gases, which were controlled and mixed by a vacuum/mass system controller (MKS 946, Andover, MA, USA). The ratio of flow rates of analytical gases and the dry synthetic air were adjusted by the relative MFC while keeping a constant total flow of 200 sccm inputting to the chamber to obtain the desired concentration of analytical gas for the gas sensing measurements. The conductometric sensing performance of the gas sensor was evaluated by measuring the resistance of the gas sensor exposed in analytical gases at a bias voltage of 1 V by a Keithley 6487 sourcemeter unit (Solon, OH, USA). The sensing response  $R$  of the gas sensor to analytical gas is defined as:

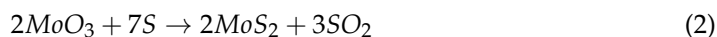
$$R (\%) = \frac{R_g - R_a}{R_g} \times 100 \quad (1)$$

where  $R_g$  and  $R_a$  are the resistance of the sensor exposed in analytical gas and synthetic air, respectively. The polarity of  $R$  is hence directly related with the direction of resistance change upon exposure to analytical gas.

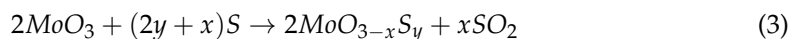
### 3. Results and Discussion

#### 3.1. Materials Characterization

The sulfurization of  $\text{MoO}_3$  in this work was carried out inside the twin-zone tube furnace as described in the Materials and Methods section by exposing as-grown  $\text{MoO}_3$  to sulfur vapor. The overall reaction of  $\text{MoO}_3$  with sulfur vapor during the sulfurization process could be described as [40–44]:



In this reaction, sulfur atoms progressively remove oxygen from  $\text{MoO}_3$  by forming gaseous  $\text{SO}_2$  whilst bonding with Mo to form  $\text{MoS}_2$ . The relative stoichiometric ratio of S to Mo at the substrate surface hence plays a significant role that will directly impact the composition of the product. Incomplete sulfurization can lead to the formation of intermediate molybdenum oxysulfides ( $\text{MoO}_{3-x}\text{S}_y$ ;  $0 \leq x \leq 3$ ;  $0 \leq y \leq 2$ ) described by the following reaction pathway [40]:



Optical microscopy and SEM were employed to characterize the evolution of morphologies of the as-prepared  $\alpha$ - $\text{MoO}_3$  nanoribbons before and after sulfurization. As shown in Figure 2a, the as-grown  $\alpha$ - $\text{MoO}_3$  samples grew randomly on the substrate with a high

density and possessed a rectangular shape with a typical length of 100  $\mu\text{m}$  and a width of 5  $\mu\text{m}$  (Figure 2c). The morphology of the  $\alpha\text{-MoO}_3$  nanoribbons is consistent with those reported earlier using the same synthesis condition [27]. The post-sulfurization directly proceeded on the surface of the as-grown  $\alpha\text{-MoO}_3$  nanoribbons in the sulfur vapor environment. After sulfurization, the samples changed in a few aspects. Firstly, the color of the nanoribbons changed from colorless (i.e., transparent) to dark violet (c.f. optical micrographs in Figure 2a,b), indicating a reduction in the optical bandgap and consistent with the color change expected for the sulfurization of  $\text{MoO}_3$  [45]. Meanwhile, the density of nanoribbons on the substrate noticeably declined, suggesting the evaporation of  $\text{MoO}_3$  that consumes the as-grown  $\text{MoO}_3$  nanoribbons. Secondly, as a result of the sulfurization, the shape of individual nanoribbons changed from elongated rectangles (Figure 2c) to irregular shapes (Figure 2d) and the edges of the crystals appeared to be less well-defined; the surface of the nanoribbons also became rougher with the presence of cracks suggesting that sulfurization alters the crystal structure of  $\text{MoO}_3$  on the surface leading to lattice mismatch among the hybrid molybdenum compounds. The morphological changes of the sulfurized  $\text{MoO}_3$  are most likely brought through a complex combination of solid-gas reaction, atomic interdiffusion, evaporation, and deposition [46]. Furthermore, the lateral size of crystals reduced significantly to about 20  $\mu\text{m}$  in length from the original length of about 100  $\mu\text{m}$ .

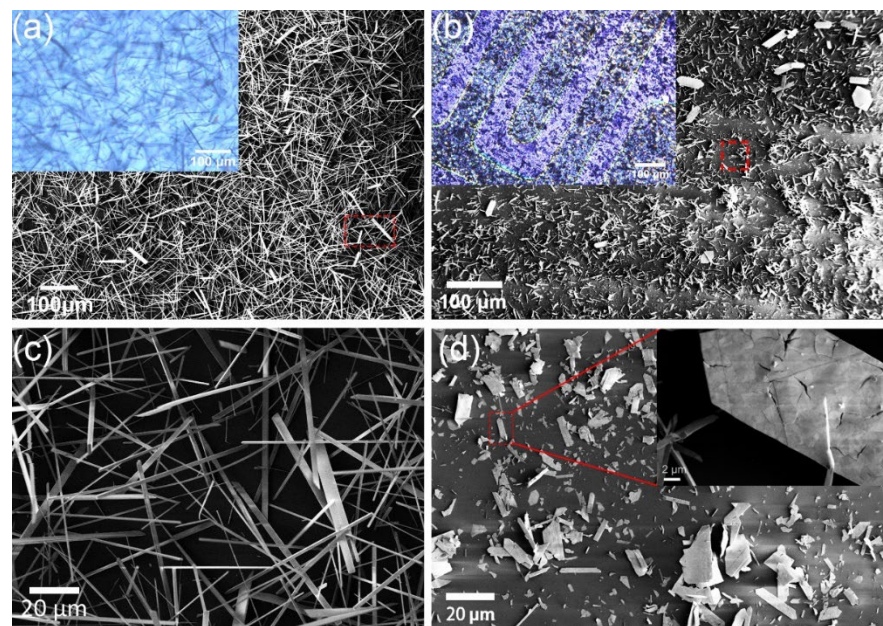


**Figure 2.** SEM image of (a) the as-grown  $\alpha\text{-MoO}_3$  nanoribbons network on  $\text{SiO}_2/\text{Si}$  interdigitated substrate, and (b) the sulfurized  $\alpha\text{-MoO}_3$  nanoribbons. Insets in (a,b) shows the corresponding optical micrographs. The high-resolution SEM image of (c) the as-grown  $\alpha\text{-MoO}_3$  and (d) the sulfurized  $\alpha\text{-MoO}_3$ . The inset in (d) is a magnified view of an individual sulfurized  $\text{MoO}_3$  nanoribbon.

High-resolution TEM images were collected to further study the structural crystallinity of the sulfurated  $\text{MoO}_3$  nanoribbons. To prepare TEM samples, substrates with sulfurized  $\text{MoO}_3$  nanoribbons were placed in ethanol to obtain a well-dispersed solution, after which droplets of the as-prepared solution were drop-casted on lacey-supported 300 mesh copper grids. Figure 3a shows a representative high-resolution transmission electron microscopy (HRTEM) image taken from the edge of sulfurized  $\text{MoO}_3$ . The lattice spacing of 0.36 nm and 0.39 nm corresponds nicely to the (001) and (100) plane of  $\alpha\text{-MoO}_3$ , whereas the lattice spacing of 0.65 nm of layers at the edge of the flake is consistent with the (002) plane of  $2\text{H-MoS}_2$ , suggesting that the outer layers of  $\alpha\text{-MoO}_3$  have been partly converted to  $\text{MoS}_2$  through the sulfurization process. The sulfurization of  $\text{MoO}_3$  has been further confirmed by

the EDS element mapping in Figure 3b which shows an even distribution of S in addition to Mo and O elements.

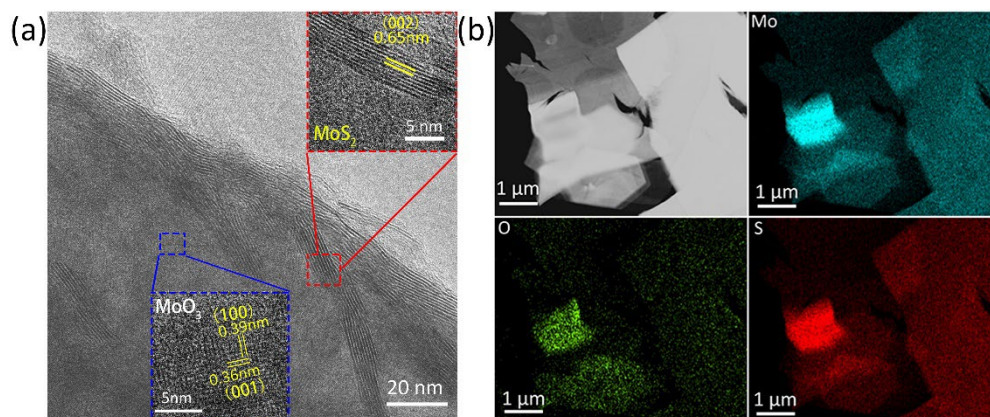


**Figure 3.** (a) TEM image and (b) EDS element mapping of the sulfurized MoO<sub>3</sub> nanoribbons.

Raman spectra were also collected to further understand the structural change of MoO<sub>3</sub> by sulfurization. As shown in Figure 4a, the Raman spectrum for as-grown MoO<sub>3</sub> (black line) exhibits the expected Raman modes for  $\alpha$ -MoO<sub>3</sub> with a layered structure [47,48]. In particular, it has well-defined Raman features associated with the vibration modes of the oxygen atoms terminating the van der Waals layer at 996 cm<sup>-1</sup> (M = O asymmetrical stretching), as well as the stretching mode of the O-Mo bonds at 818 cm<sup>-1</sup> for the corner-shared oxygen and at 666 cm<sup>-1</sup> for the edge-shared, triply bonded oxygen [49,50]. After sulfurization, the Raman spectrum (red line) displays new peaks in addition to retaining the majority of the characteristic features of MoO<sub>3</sub>. Most notably, the new peaks at 381 cm<sup>-1</sup> and 406 cm<sup>-1</sup> are consistent with the characteristic in-plane  $E_{2g}^1$  vibration mode and the out-of-plane  $A_{1g}$  vibration mode of 2H-MoS<sub>2</sub>, respectively [46,51]. The two Raman peaks have a frequency difference of ~25 cm<sup>-1</sup>, suggesting that the MoS<sub>2</sub> on the surface of MoO<sub>3</sub> is multilayer, which is consistent with the HRTEM results. Moreover, the peak 454 cm<sup>-1</sup> is assigned to the second order 2LA(M) phonons of MoS<sub>2</sub> which are generally present in multilayers of MoS<sub>2</sub> [52,53]. There are, however, additional Raman peaks that cannot be exclusively assigned to MoO<sub>3</sub> or MoS<sub>2</sub>, such as strong Raman features at 198, 222, 560, and 730 cm<sup>-1</sup>, and they are best assigned to the vibration modes of Mo-O and Mo-S bonds in intermediate compound molybdenum oxysulfide (MoO<sub>3-x</sub>S<sub>y</sub>) as a result of incomplete sulfurization described in the reaction in Equation (2) [40]. The co-existence of MoO<sub>3</sub>, MoS<sub>2</sub>, and the intermediate molybdenum oxysulfide is further corroborated by XRD. Figure 4b shows the XRD patterns of MoO<sub>3</sub> before (black line) and after (red line) sulfurization. The intense diffraction peaks of pristine MoO<sub>3</sub> can all be indexed to the orthorhombic  $\alpha$ -MoO<sub>3</sub> (JCPDS Card No. 00-005-0508) including the (0 2 0) and (0 4 0) planes that are characteristic for layered MoO<sub>3</sub> [27,54,55]. After sulfurization, the XRD patterns display several additional diffraction peaks including the diffraction peaks with 2 $\theta$  at 14.4°, 39.5°, and 44.3° corresponding to reflections of the (002), (103), and (006) planes of 2H-MoS<sub>2</sub> (JCPDS No. 00-037-1492) [44,56], confirming again the formation of MoS<sub>2</sub> on the MoO<sub>3</sub> nanoribbons after sulfurization. With the 2 $\theta$  position of the (002) diffraction peak and the wavelength of Cu K $\alpha$  line ( $\lambda = 0.15418$  nm), we can arrive at an interlayer distance of 0.62 nm for MoS<sub>2</sub>, in good agreement with the d-spacing determined by HRTEM in Figure 3a. The formation of intermediate MoO<sub>3-x</sub>S<sub>y</sub> is also supported by the appearance of additional XRD patterns consistent with those from a representative molybdenum oxysulfide MoS<sub>0.12</sub>O<sub>1.88</sub> (JCPDS No. 04-007-8381).

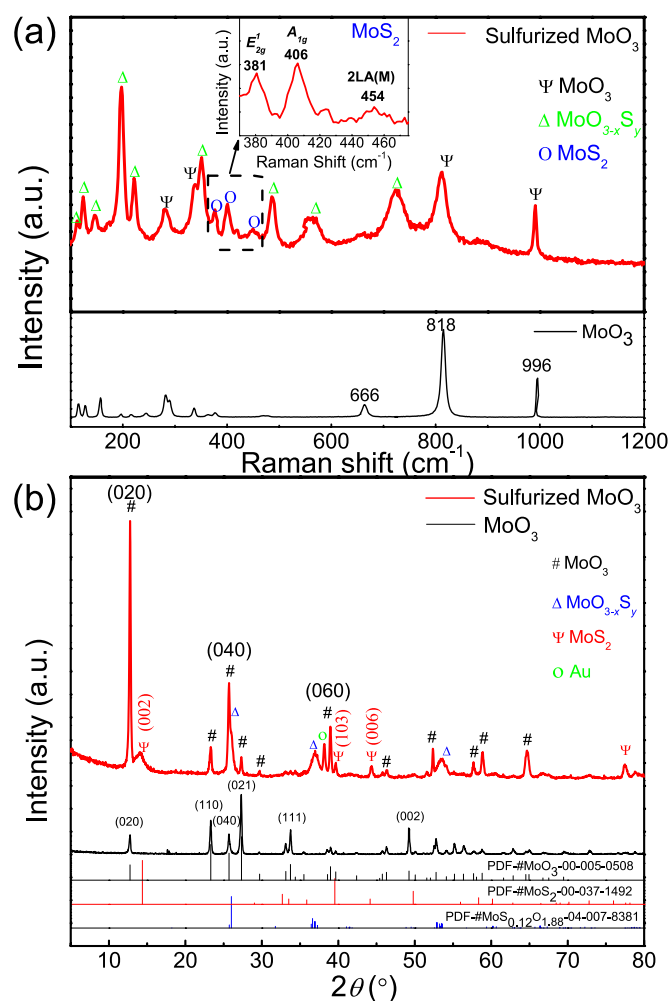


**Figure 4.** (a) Raman spectra and (b) XRD patterns of  $\text{MoO}_3$  on  $\text{SiO}_2/\text{Si}$  substrate before and after sulfurization.

X-ray photoelectron spectroscopy (XPS) characterization was also carried out to determine the compositions and valence states of sulfurized  $\text{MoO}_3$ . The binding energy of XPS spectra was calibrated using adventitious carbon (284.8 eV) as a reference. As shown in the wide survey scan in Figure S1, no other unexpected contaminants were introduced after sulfurization. Figure 5a shows the  $\text{Mo } 3d$  core-level spectrum which can be deconvoluted to three distinct  $3d$  spin-orbit split doublets fitted by a Voigt line shape. The XPS doublets dominating the high binding energy part of the spectrum at 236.1 eV ( $\text{Mo } 3d_{3/2}$ ) and 233.0 eV ( $\text{Mo } 3d_{5/2}$ ) are assigned to the characteristic  $\text{Mo}^{6+}$  state in  $\alpha\text{-MoO}_3$  [57]. Meanwhile, the  $\text{Mo } 3d$  doublets positioned at 232.4 and 229.3 eV are consistent with  $\text{Mo}^{4+}$  in  $2\text{H-MoS}_2$ , with the accompanied  $\text{S } 2s$  peak at 226.5 eV [58,59]. The  $\text{Mo } 3d$  doublets at 234.9 eV ( $\text{Mo } 3d_{3/2}$ ) and 231.8 eV ( $\text{Mo } 3d_{5/2}$ ), located in between those of the  $\text{Mo}^{6+}$  and  $\text{Mo}^{4+}$  components, can be ascribed to  $\text{Mo}$  in  $\text{MoO}_{3-x}\text{S}_y$  with a nominal oxidation state of  $5^+$  [24,60]. Correspondingly,  $\text{S } 2p$  core-level spectrum in Figure 5b shows the  $\text{S } 2p$  doublets at 163.2 eV ( $\text{S } 2p_{1/2}$ ) and 162.1 eV ( $\text{S } 2p_{3/2}$ ) originating from  $\text{Mo-S}$  bonds in  $2\text{H-MoS}_2$  [35,36,42]. In addition, the peaks at 169.7 eV ( $\text{S } 2p_{1/2}$ ) and 168.6 eV ( $\text{S } 2p_{3/2}$ ) correspond to the  $\text{S-O}$  bonds both in the intermediate molybdenum oxysulfide and potentially the adsorbed  $\text{SO}_2$  on the surface of  $\text{MoO}_3$  as a result of the sulfurization reaction [51,61,62].

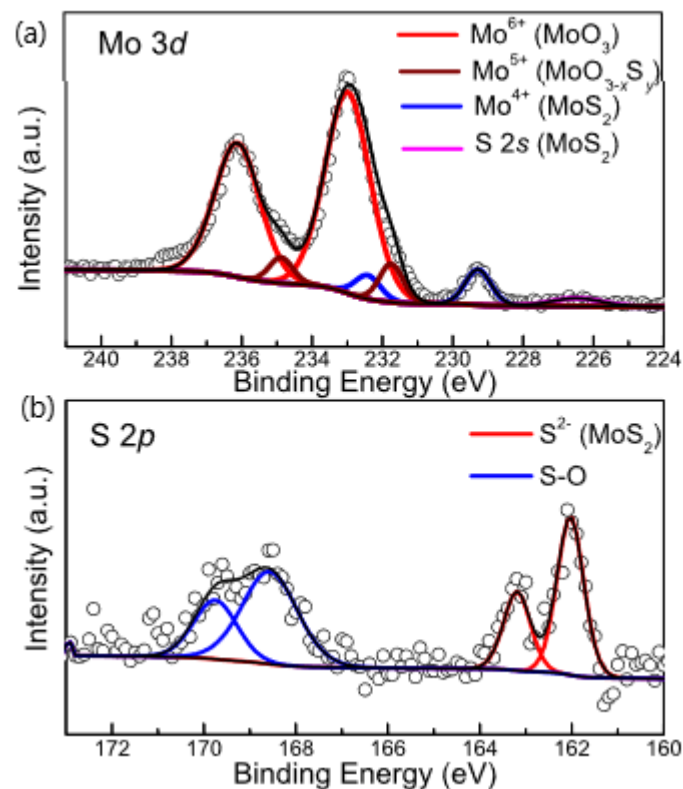


**Figure 5.** XPS spectra of (a) Mo 3d core-levels and (b) S 2p core-levels of sulfurized MoO<sub>3</sub> on SiO<sub>2</sub>/Si substrate.

The above structural and compositional analysis shows that the sulfurization process induces the formation of MoO<sub>3</sub>/MoS<sub>2</sub> hybrid core-shell structure with the co-existence of incompletely sulfurized oxysulfide intermediates embedded on the surface, as shown schematically in Figure 6. Because of the relatively high temperature of the sulfurization process, the reaction also involves evaporation of MoO<sub>3</sub> and re-deposition which consume the initial MoO<sub>3</sub> nanoribbons, giving rise to the reduced lateral dimensions and morphological changes of sulfurized MoO<sub>3</sub> as discussed above. Although the overall molar ratio of S:MoO<sub>3</sub> for the respective sources exceeds the required ratio of 7:2 as in reaction Equation (1) for complete sulfurization, at regions where the high-density MoO<sub>3</sub> nanoribbons overlap inhibiting the flow of S vapor to react completely with the outer layers of MoO<sub>3</sub>, the local effective ratio could be lower leading to the formation of incompletely sulfurized oxysulfide intermediates.

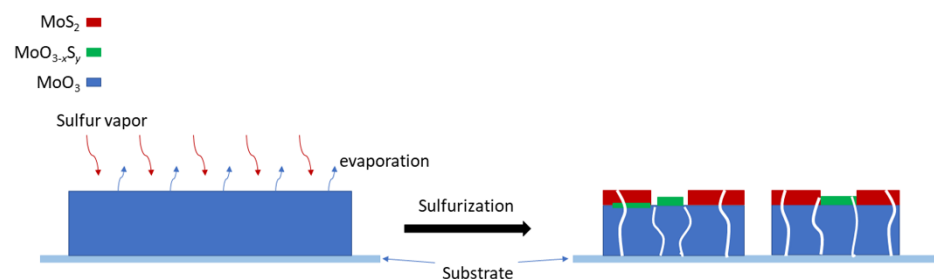


**Figure 6.** A schematic diagram illustrating the sulfurization process of MoO<sub>3</sub> nanoribbons.

Because NO<sub>2</sub> carries a magnetic moment originating from its unpaired valence electron, the magnetic properties of sensing layers could potentially benefit gas sensing performance by enhancing affinity to substrates through magnetic dipole interactions [63]. Although both  $\alpha$ -MoO<sub>3</sub> and MoS<sub>2</sub> are intrinsically non-magnetic, ferromagnetism could be intro-

duced through defects, edges, and non-stoichiometry that induce unpaired electrons in Mo 4d orbitals [64–68]. We therefore measured the magnetic properties of the sulfurated MoO<sub>3</sub> samples by VSM with an applied magnetic field in the range of –5 T to 5 T. Figure 7 presents a comparison of the magnetization vs. magnetic field for sulfurated MoO<sub>3</sub> samples at room temperature and 10 K and the pristine MoO<sub>3</sub>. The pristine MoO<sub>3</sub> nanoribbons do not exhibit any hysteretic behaviors, consistent with its non-magnetic character with a Mo 4d<sup>0</sup> configuration. After sulfurization, the MoS<sub>2</sub>@MoO<sub>3</sub> sample clearly shows ferromagnetic behavior with a specific saturation magnetization (M<sub>s</sub>) about 0.05 emu/g at room temperature. The saturation magnetization at 10 K is comparable with that of room temperature, but it further increases slightly with at large magnetic field and did not saturate up to 5 T. This magnetization behavior suggests a combination of ferromagnetic and paramagnetic properties. The observed ferromagnetism is comparable to those reported for defective MoS<sub>2</sub> and MoO<sub>3</sub> with defect-induced ferromagnetism [64,65,69], and therefore could also originate from the prevalent defects as a result of the sulfurization process. In addition, the edges of MoS<sub>2</sub> have been shown to display robust ferromagnetism [70]; the MoS<sub>2</sub> nanosheets that cover the surface of MoO<sub>3</sub> are expected to give rise to plenty of edge states that enhance the ferromagnetism. Furthermore, the existence of Mo<sup>5+</sup> with an unpaired 4d electron (4d<sup>1</sup> configuration), as revealed in Figure 5a by XPS, could also provide magnetic moments for the sulfurized MoS<sub>2</sub>@MoO<sub>3</sub> hybrid structures [65]. Lastly, interface-induced ferromagnetism due to interfacial charge transfer [66] could also occur at the MoS<sub>2</sub>@MoO<sub>3</sub> heterointerface by introducing spin magnetic moments into the Mo-4d conduction bands of MoO<sub>3</sub>. It is worth noting that some of the magnetic moments introduced by sulfurization could be isolated lacking long-range ferromagnetic coupling, giving rise to the observed paramagnetic behavior as mentioned above.

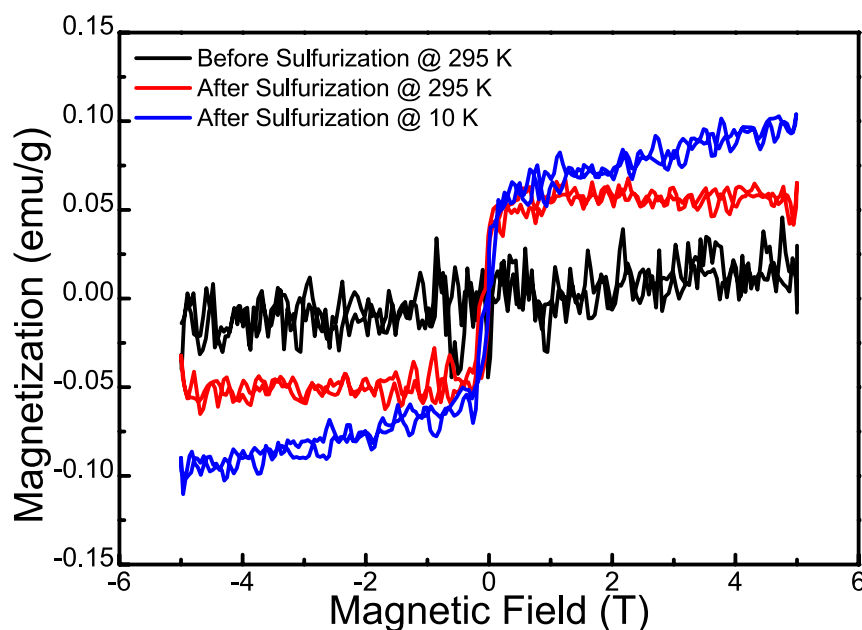


**Figure 7.** Magnetic hysteresis loop of pristine MoO<sub>3</sub> and sulfurized MoO<sub>3</sub> at different temperatures.

### 3.2. Gas-Sensing Performance

The gas sensor was fabricated by depositing electrodes on SiO<sub>2</sub>/Si substrates before  $\alpha$ -MoO<sub>3</sub> synthesis and the subsequent sulfurization. The gas-sensing performance for NO<sub>2</sub>, including the dynamic sensing response, response and recovery time, reversibility, and selectivity of the sulfurized MoO<sub>3</sub> gas sensors was evaluated with the multichannel gas sensing system (see Figure S2 for the schematics of the sensing test system). All the data for the gas sensing performance were collected at the optimal operating temperature of 125 °C, which was determined by measuring the sensing response as a function of

the working temperature of the sensors which was controlled via the ceramic heater underneath. In contrast to positive responses (i.e., increase of resistance) upon exposure to NO<sub>2</sub> (typical oxidizing gas) usually displayed by metal oxide conductometric gas sensors including  $\alpha$ -MoO<sub>3</sub> [10,27,71], the sulfurized device displays a *p*-type response (i.e., decrease of resistance shown in Figure S3) to NO<sub>2</sub> with a concentration in the range of 0.5 ppm to 10 ppm (Figure 8a). The device presents a maximum negative response of  $-30.1\%$  to NO<sub>2</sub> at 10 ppm and a small but noticeable response of  $-4.3\%$  to 0.5 ppm of NO<sub>2</sub>. The dependence of response on NO<sub>2</sub> concentration is displayed in the inset of Figure 8a which deviates from a linear dependence at high concentration, suggesting the adsorption of NO<sub>2</sub> on the surface of sulfurized MoO<sub>3</sub> starts to be limited at high concentration. According to the dependence at the low concentrations (inset I of Figure 8a), we can also determine a limit of detection (LOD) of  $\sim 0.15$  ppm by implementing the IUPAC method [72]. Intriguingly, the sensors display a small positive response upon the input of NO<sub>2</sub> before the dominating negative response (inset II of Figure 8a), the origin of which will be discussed below. Figure 8b illustrates the response time ( $\tau_{\text{res}}$ ) and recovery time ( $\tau_{\text{rec}}$ ) of the device based on MoS<sub>2</sub>@MoO<sub>3</sub> towards NO<sub>2</sub> from 0.5 ppm to 10 ppm at the optimal temperature of 125 °C (also see Figure S4 of Supplementary Material for a detailed presentation of response and recovery time to 10 ppm NO<sub>2</sub>). In general, the response time decreases with increasing concentration of NO<sub>2</sub> (<5 ppm) whereas the recovery time exhibits an opposite trend. Similar dependence has been reported before and is explained with the Freundlich law which dictates a higher diffusion and reaction process with NO<sub>2</sub> molecules adsorption (hence faster response dynamics) on the surface at a higher concentration [73,74]. The corresponding desorption is also going to take longer at higher concentration because of the higher number of adsorbed molecules. Intriguingly, the response time at the highest concentration of 10 ppm experiences an increase. It is not exactly clear what causes this anomaly that deviates from the Freundlich law. One possible cause is the initial positive response spike following gas introduction that goes into the calculation of response time (Figure S4). At high NO<sub>2</sub> concentration, the positive response spike also increases in magnitude and may cause the negative response to take longer to reach its maximum value. It is worth noting that the nominal response and recovery time of our sensors tend to be overestimated due to the set-up of the sensing test chamber with a large internal volume of 1100 mL. It therefore requires a significantly extended duration to completely replace this volume with the analytical gas at the desired concentration and to purge it away to return to the baseline [27]. However, their dependence on gas concentration (as presented in Figure 8b) is still relevant. The reproducibility and reversibility of the gas sensors are also presented in Figure 8c, in which the device operated with NO<sub>2</sub> at 0.5 ppm in four consecutive cycles over an 8 h testing period. The sensors show a reproducible response with a standard deviation of response less than 0.4%. The long-term stability of this sensor was also measured for 8 weeks (Figure S5), in which the response to NO<sub>2</sub> decreased from  $-30.1\%$  to  $-23\%$  in the first week and then it kept a relatively stable response about  $-22\%$  in 7 weeks. Lastly, the selectivity of the sulfurized MoO<sub>3</sub> sensors was studied by measuring responses to a few interference gases including N<sub>2</sub>O, NH<sub>3</sub>, CO, and ethanol (ETH) as shown in Figure 8d. All the responses to the analytical gases were collected at 10 ppm concentration. The MoS<sub>2</sub>@MoO<sub>3</sub> gas sensors clearly exhibit a good selectivity to NO<sub>2</sub>; we attribute the selectivity to the enhanced magnetic interaction between the paramagnetic NO<sub>2</sub> and the ferromagnetic MoS<sub>2</sub>@MoO<sub>3</sub> sensing layer. Upon NO<sub>2</sub> adsorption, it induces additional magnetic dipole interaction with the substrate in addition to a surface electric dipole (due to the polar character of NO<sub>2</sub>), giving rise to a stronger adsorption affinity than the other non-magnetic interference gas molecules.

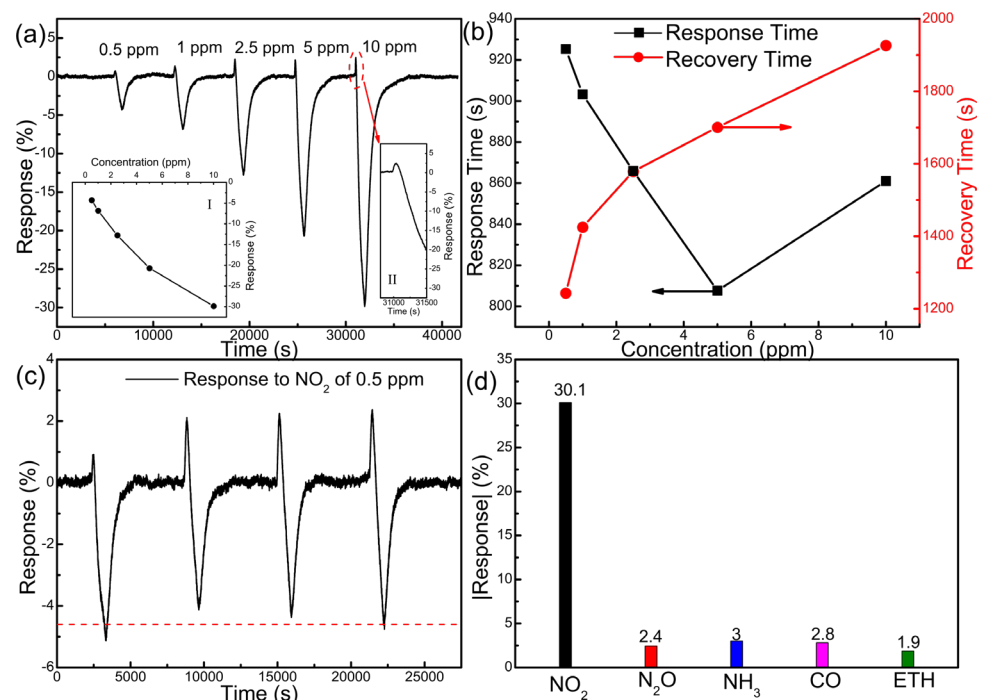


**Figure 8.** (a) Dynamic sensing response of the MoS<sub>2</sub>@MoO<sub>3</sub> based sensor to NO<sub>2</sub> at concentrations ranging from 0.5 ppm to 10 ppm under the working temperature of 125 °C. Inset I is a plot of the sensing response as a function of NO<sub>2</sub> concentration and inset II is the enlarged view of the initial positive response to 10 ppm NO<sub>2</sub>. (b) Response and recovery time of the MoS<sub>2</sub>@MoO<sub>3</sub>-based sensor toward NO<sub>2</sub> from 0.5 ppm to 10 ppm at the working temperature of 125 °C. (c) Cyclic response of the sensor toward 0.5 ppm NO<sub>2</sub>. (d) Selectivity of the sensor in absolute response to NO<sub>2</sub>, N<sub>2</sub>O, NH<sub>3</sub>, CO, and ETH of 10 ppm concentration. Measurements were performed at the optimal operating temperature of 125 °C.

### 3.3. Gas-Sensing Mechanism

Both  $\alpha$ -MoO<sub>3</sub> and MoS<sub>2</sub> are typical n-type semiconductors due to the prevalence of anion vacancies (i.e., O and S vacancies) in their pristine structure due to their low formation energy [75,76]. Anion vacancies act as shallow donors in the bandgap leading to n-type conduction behavior. It is well accepted that n-type semiconductors usually respond to oxidizing gas such as NO<sub>2</sub> with an increase in resistance (i.e., positive response) as a result of electron depletion in the sensing materials following electron transfer to analytical gas molecules facilitated through the surface adsorbed oxygen ions [77]. The reversal of the response polarity (i.e., decrease in resistance) to NO<sub>2</sub> in our MoS<sub>2</sub>@MoO<sub>3</sub> hybrid sensors is therefore intriguing. Due to an extremely high electron affinity of 6.7 eV [75,78], MoO<sub>3</sub> is a potent electron acceptor and has been widely used as an interfacial layer to induce or enhance *p*-type conduction in a wide range of electronic materials including organic semiconductors, diamond, graphene, and TMDCs through the charge transfer doping process [79]. We therefore attribute the negative sensing response to the heterointerface formed between MoO<sub>3</sub> and MoS<sub>2</sub> with the concomitant interfacial charge exchange. As illustrated in the schematic energy band diagram in Figure 9, MoS<sub>2</sub> has an ionization energy of ~5.6 eV [80], and it therefore forms a type-III broken-gap heterojunction with MoO<sub>3</sub> with a much deeper conduction band. Because of this extreme band offset, electrons flow spontaneously from the valance band of MoS<sub>2</sub> to the conduction band of MoO<sub>3</sub> until the Fermi level is equated at thermodynamic equilibrium [81], leading to strong band bending across the interface. The interfacial electron transfer not only depletes the initial free electron carriers in MoS<sub>2</sub> but also moves the Fermi energy further to form a MoS<sub>2</sub> inversion layer with *p*-type character [82]. When exposed to air, the hole accumulation

layer in MoS<sub>2</sub> is enhanced because of further electron transfer from the MoS<sub>2</sub> to adsorbed oxygen molecules to form different negative oxygen ion species (O<sub>2</sub><sup>-</sup> and O<sup>-</sup>) [83,84].

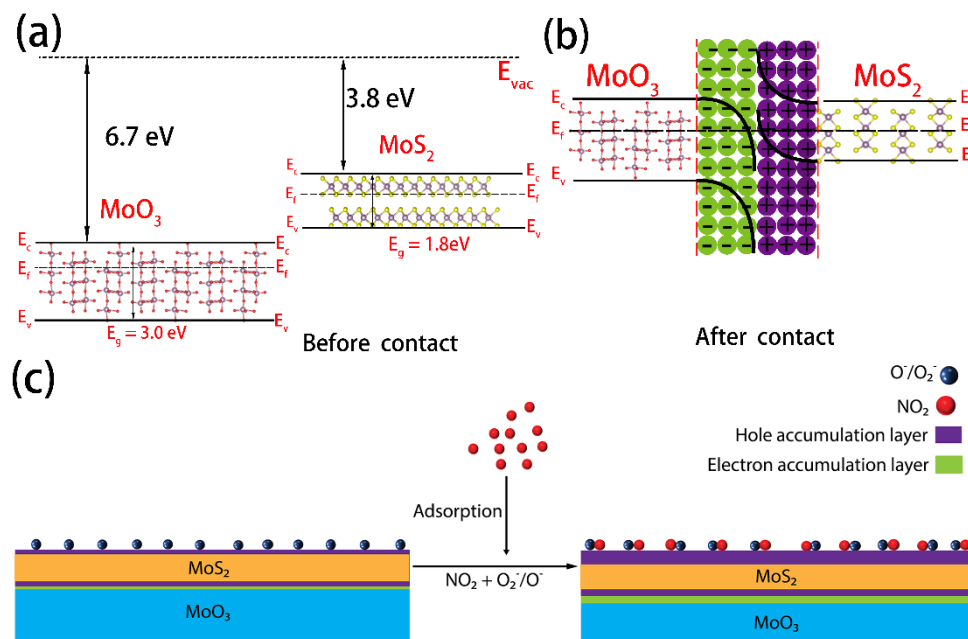
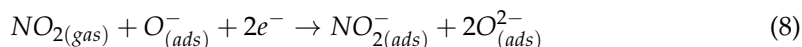
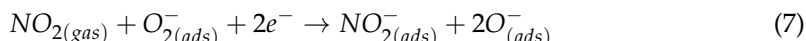
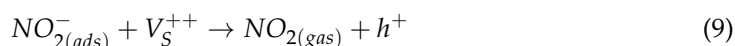


**Figure 9.** The energy band diagram of MoS<sub>2</sub>@MoO<sub>3</sub> heterostructure (a) before contact, (b) after contact; (c) gas-sensing mechanism of MoS<sub>2</sub>@MoO<sub>3</sub> heterostructure.

Upon exposure to NO<sub>2</sub>, the adsorbed NO<sub>2</sub> molecules directly interact with MoS<sub>2</sub> or through the negative oxygen ion species to capture electrons, accompanied by further hole generating in MoS<sub>2</sub> [85,86]:



In addition, NO<sub>2</sub> can also interact with S vacancies (V<sub>S</sub><sup>++</sup>) at the surface MoS<sub>2</sub> [84], again generating holes into the valance band [83,85–87].



Consequently, the hole accumulation layer in MoS<sub>2</sub> is further enlarged with concomitant increase of hole density, which is translated into a decrease of resistance in response to NO<sub>2</sub>.

It is worth noting that the resistance change of the n-type α-MoO<sub>3</sub> upon NO<sub>2</sub> adsorption should remain positive and counteract the resistance change of the p-type MoS<sub>2</sub> hole accumulation layer. This may explain the positive response spike immediately following NO<sub>2</sub> introduction as in Figure 8a. However, since the thickness of MoS<sub>2</sub> is expected to be much lower than that of MoO<sub>3</sub> and comparable to the Debye length, its sensing response is maximized to dominate the overall sensing behavior [77], thereby resulting in a net decrease of resistance (i.e., negative response). Similar phenomena have been observed in other materials (e.g., a-RP [88], SnO<sub>2</sub> [89], and CuO/ZnO [90]).

#### 4. Conclusions

In conclusion, we report MoS<sub>2</sub>@MoO<sub>3</sub> ferromagnetic heterostructure synthesized by post-sulfurization of  $\alpha$ -MoO<sub>3</sub> nanoribbons on SiO<sub>2</sub>/Si substrate. Gas sensors fabricated with the sulfurized MoO<sub>3</sub> as sensing layers MoS<sub>2</sub>@MoO<sub>3</sub> display a *p*-type response towards NO<sub>2</sub> with high sensitivity in the range of 0.5 ppm to 10 ppm with a LOD of ~0.15 ppm at the optimal working temperature of 125 °C. The response and recovery time of the sensors, although sluggish due to the nature of the testing apparatus, generally follows the Freundlich model which governs the gas adsorption and diffusion on the surface. The gas sensor also presents good reversibility and impressive selectivity against interfering gases including N<sub>2</sub>O, NH<sub>3</sub>, CO, and ETH. The energy band offset at the MoS<sub>2</sub>-MoO<sub>3</sub> heterojunction results in interfacial charge transfer leading to a *p*-type inversion layer in MoS<sub>2</sub>, and the gas sensing mechanism can be explained by the charge transfer between the analytical gas molecules and the *p*-type MoS<sub>2</sub> inversion layer at the MoS<sub>2</sub>-MoO<sub>3</sub> heterojunction. The efficient sensing performance for NO<sub>2</sub> can be attributed to the enhanced affinity between the paramagnetic NO<sub>2</sub> molecules and the ferromagnetic sensing layer. This work demonstrates a promising gas-sensing platform based on MoS<sub>2</sub>@MoO<sub>3</sub> heterostructures and could also have implications for broader applications that utilize the unique electronic and magnetic properties of hybrid 2D metal-oxide/TMDCs heterostructures.

**Supplementary Materials:** The following supporting information can be downloaded at: <https://www.mdpi.com/article/10.3390/nano12081303/s1>, Figure S1. XPS wide survey spectrum of sulfurized MoO<sub>3</sub>, Figure S2. Schematic illustration for the multi-channel gas-sensing characterization system. Inset shows an optical image of the MoS<sub>2</sub>@MoO<sub>3</sub>-based gas sensors. Figure S3. Transient resistance of MoS<sub>2</sub>@MoO<sub>3</sub>-based gas sensor towards NO<sub>2</sub> in range of 0.5 ppm to 10 ppm. Figure S4. Response (0–90%) and recovery time (100–10%) of the MoS<sub>2</sub>@MoO<sub>3</sub>-based sensor to 10 ppm NO<sub>2</sub> at 125 °C. Figure S5. Long-term stability of MoS<sub>2</sub>@MoO<sub>3</sub> sensors towards 10 ppm NO<sub>2</sub> under the operating temperature of 125 °C over a period of 56 days.

**Author Contributions:** Conceptualization, W.L. and D.-C.Q.; formal analysis, W.L.; funding acquisition, N.M. and D.-C.Q.; investigation, W.L.; methodology, W.L. and M.S.; resources, D.-C.Q.; supervision, T.T., N.M. and D.-C.Q.; visualization, W.L. and K.X.; writing—original draft, W.L.; writing—review and editing, M.S., K.X., T.T. and N.M. All authors have read and agreed to the published version of the manuscript.

**Funding:** This research is funded by the Australian Research Council (Grant No. FT160100207) (Grant No. DP200102546).

**Institutional Review Board Statement:** Not applicable.

**Informed Consent Statement:** Not applicable.

**Data Availability Statement:** Not applicable.

**Acknowledgments:** Some of the data reported in this work were obtained at the Central Analytical Research Facility (CARF) at the Queensland University of Technology (QUT). The authors acknowledge the continuous support from QUT through the Centre for Materials Science.

**Conflicts of Interest:** The authors declare no conflict of interest.

#### References

1. Bernstein, J.A.; Alexis, N.; Barnes, C.; Bernstein, I.L.; Nel, A.; Peden, D.; Diaz-Sanchez, D.; Tarlo, S.M.; Williams, P.B.; Bernstein, J.A. Health effects of air pollution. *J. Allergy Clin. Immunol.* **2004**, *114*, 1116–1123. [[CrossRef](#)] [[PubMed](#)]
2. Bernstein, J.A.; Alexis, N.; Bacchus, H.; Bernstein, I.L.; Fritz, P.; Horner, E.; Li, N.; Mason, S.; Nel, A.; Oullette, J.; et al. The health effects of nonindustrial indoor air pollution. *J. Allergy Clin. Immunol.* **2008**, *121*, 585–591. [[CrossRef](#)] [[PubMed](#)]
3. Das, A.; Dost, R.; Richardson, T.; Grell, M.; Morrison, J.J.; Turner, M.L. A Nitrogen Dioxide Sensor Based on an Organic Transistor Constructed from Amorphous Semiconducting Polymers. *Adv. Mater.* **2007**, *19*, 4018–4023. [[CrossRef](#)]
4. Fernández-Sánchez, J.F.; Fernández, I.; Steiger, R.; Beer, R.; Cannas, R.; Spichiger-Keller, U.E. Second Generation Nanostructured Metal Oxide Matrices to Increase the Thermal Stability of CO and NO<sub>2</sub> Sensing Layers Based on Iron(II) Phthalocyanine. *Adv. Funct. Mater.* **2007**, *17*, 1188–1198. [[CrossRef](#)]

5. Donarelli, M.; Prezioso, S.; Perrozzi, F.; Bisti, F.; Nardone, M.; Giancaterini, L.; Cantalini, C.; Ottaviano, L. Response to NO<sub>2</sub> and other gases of resistive chemically exfoliated MoS<sub>2</sub>-based gas sensors. *Sens. Actuator B Chem.* **2015**, *207*, 602–613. [[CrossRef](#)]
6. Ji, S.; Wang, H.; Wang, T.; Yan, D. A High-Performance Room-Temperature NO<sub>2</sub> Sensor Based on An Ultrathin Heterojunction Film. *Adv. Mater.* **2013**, *25*, 1755–1760. [[CrossRef](#)] [[PubMed](#)]
7. Kumar, S.; Pavelyev, V.; Mishra, P.; Tripathi, N.; Sharma, P.; Calle, F. A review on 2D transition metal di-chalcogenides and metal oxide nanostructures based NO<sub>2</sub> gas sensors. *Mater. Sci. Semicond. Process.* **2020**, *107*, 104865. [[CrossRef](#)]
8. Korotcenkov, G.; Brinzari, V.; Cho, B.K. Conductometric gas sensors based on metal oxides modified with gold nanoparticles: A review. *Microchim. Acta* **2016**, *183*, 1033–1054. [[CrossRef](#)]
9. Geeta Rani, B.; Saisri, R.; Kailasa, S.; Sai Bhargava Reddy, M.; Maseed, H.; Venkateswara Rao, K. Architectural tailoring of orthorhombic MoO<sub>3</sub> nanostructures toward efficient NO<sub>2</sub> gas sensing. *J. Mater. Sci.* **2020**, *55*, 8109–8122. [[CrossRef](#)]
10. Rahman, F.; Zavabeti, A.; Rahman, M.A.; Arash, A.; Mazumder, A.; Walia, S.; Sriram, S.; Bhaskaran, M.; Balendhran, S. Dual Selective Gas Sensing Characteristics of 2D  $\alpha$ -MoO<sub>3-x</sub> via a Facile Transfer Process. *ACS Appl. Mater. Interfaces* **2019**, *11*, 40189–40195. [[CrossRef](#)]
11. Yang, S.X.; Jiang, C.B.; Wei, S.H. Gas sensing in 2D materials. *Appl. Phys. Rev.* **2017**, *4*, 021304. [[CrossRef](#)]
12. Di Bartolomeo, A. Emerging 2D Materials and Their Van Der Waals Heterostructures. *Nanomaterials* **2020**, *10*, 579. [[CrossRef](#)] [[PubMed](#)]
13. Joshi, N.; Hayasaka, T.; Liu, Y.; Liu, H.; Oliveira, O.N.; Lin, L. A review on chemiresistive room temperature gas sensors based on metal oxide nanostructures, graphene and 2D transition metal dichalcogenides. *Microchim. Acta* **2018**, *185*, 213. [[CrossRef](#)] [[PubMed](#)]
14. Li, Z.; Qiao, H.; Guo, Z.; Ren, X.; Huang, Z.; Qi, X.; Dhanabalan, S.C.; Ponraj, J.S.; Zhang, D.; Li, J.; et al. High-Performance Photo-Electrochemical Photodetector Based on Liquid-Exfoliated Few-Layered InSe Nanosheets with Enhanced Stability. *Adv. Funct. Mater.* **2018**, *28*, 1705237. [[CrossRef](#)]
15. Zhang, L.; Khan, K.; Zou, J.; Zhang, H.; Li, Y. Recent Advances in Emerging 2D Material-Based Gas Sensors: Potential in Disease Diagnosis. *Adv. Mater. Interfaces* **2019**, *6*, 1901329. [[CrossRef](#)]
16. Donarelli, M.; Ottaviano, L. 2D Materials for Gas Sensing Applications: A Review on Graphene Oxide, MoS<sub>2</sub>, WS<sub>2</sub> and Phosphorene. *Sensors* **2018**, *18*, 3638. [[CrossRef](#)] [[PubMed](#)]
17. Novoselov, K.S.; Mishchenko, A.; Carvalho, A.; Castro Neto, A.H. 2D materials and van der Waals heterostructures. *Science* **2016**, *353*, aac9439. [[CrossRef](#)]
18. Cao, R.; Zhou, B.; Jia, C.; Zhang, X.; Jiang, Z. Theoretical study of the NO, NO<sub>2</sub>, CO, SO<sub>2</sub>, and NH<sub>3</sub> adsorptions on multi-diameter single-wall MoS<sub>2</sub> nanotube. *J. Phys. D Appl. Phys.* **2015**, *49*, 045106. [[CrossRef](#)]
19. Bermudez, V.M. Computational Study of the Adsorption of NO<sub>2</sub> on Monolayer MoS<sub>2</sub>. *J. Phys. Chem. C* **2020**, *124*, 15275–15284. [[CrossRef](#)]
20. Zheng, W.; Xu, Y.; Zheng, L.; Yang, C.; Pinna, N.; Liu, X.; Zhang, J. MoS<sub>2</sub> Van der Waals p–n Junctions Enabling Highly Selective Room-Temperature NO<sub>2</sub> Sensor. *Adv. Funct. Mater.* **2020**, *30*, 2000435. [[CrossRef](#)]
21. Hau, H.H.; Duong, T.T.H.; Man, N.K.; Thi Viet Nga, T.; Thi Xuan, C.; Thi Thanh Le, D.; Van Toan, N.; Hung, C.M.; Van Duy, N.; Van Hieu, N.; et al. Enhanced NO<sub>2</sub> gas-sensing performance at room temperature using exfoliated MoS<sub>2</sub> nanosheets. *Sens. Actuators A Phys.* **2021**, *332*, 113137. [[CrossRef](#)]
22. Kumbhakar, P.; Chowde Gowda, C.; Mahapatra, P.L.; Mukherjee, M.; Malviya, K.D.; Chaker, M.; Chandra, A.; Lahiri, B.; Ajayan, P.M.; Jariwala, D.; et al. Emerging 2D metal oxides and their applications. *Mater. Today* **2021**, *45*, 142–168. [[CrossRef](#)]
23. Wu, D.; Qi, D.; Liu, J.; Wang, Z.; Hao, Q.; Hong, G.; Liu, F.; Ouyang, F.; Zhang, W. Growth of centimeter-scale single crystal MoO<sub>3</sub> ribbons for high performance ultraviolet photodetectors. *Appl. Phys. Lett.* **2021**, *118*, 243101. [[CrossRef](#)]
24. Duraisamy, S.; Ganguly, A.; Sharma, P.K.; Benson, J.; Davis, J.; Papakonstantinou, P. One-Step Hydrothermal Synthesis of Phase-Engineered MoS<sub>2</sub>/MoO<sub>3</sub> Electrocatalysts for Hydrogen Evolution Reaction. *ACS Appl. Nano Mater.* **2021**, *4*, 2642–2656. [[CrossRef](#)]
25. He, R.; Lai, H.; Wang, S.; Chen, T.; Xie, F.; Chen, Q.; Liu, P.; Chen, J.; Xie, W. Few-layered vdW MoO<sub>3</sub> for sensitive, uniform and stable SERS applications. *Appl. Surf. Sci.* **2020**, *507*, 145116. [[CrossRef](#)]
26. Du, Y.; He, J.; Hou, G.; Yuan, F.  $\alpha$ -MoO<sub>3</sub> sheets with high exposed plane reinforced by thermal plasma for stable Li-ion storage. *Electrochim. Acta* **2020**, *334*, 135593. [[CrossRef](#)]
27. Li, W.; Xing, K.; Liu, P.; Chuang, C.; Lu, Y.-R.; Chan, T.-S.; Tesfamichael, T.; Motta, N.; Qi, D.-C. Ultrasensitive NO<sub>2</sub> Gas Sensors Based on Layered  $\alpha$ -MoO<sub>3</sub> Nanoribbons. *Adv. Mater. Technol.* **2021**, 2100579. [[CrossRef](#)]
28. Balendhran, S.; Walia, S.; Nili, H.; Ou, J.Z.; Zhuiykov, S.; Kaner, R.B.; Sriram, S.; Bhaskaran, M.; Kalantar-zadeh, K. Two-Dimensional Molybdenum Trioxide and Dichalcogenides. *Adv. Funct. Mater.* **2013**, *23*, 3952–3970. [[CrossRef](#)]
29. Malik, R.; Joshi, N.; Tomer, V.K. Advances in the designs and mechanisms of MoO<sub>3</sub> nanostructures for gas sensors: A holistic review. *Mater. Adv.* **2021**, *2*, 4190–4227. [[CrossRef](#)]
30. Wei, Z.; Hai, Z.; Akbari, M.K.; Qi, D.; Xing, K.; Zhao, Q.; Verpoort, F.; Hu, J.; Hyde, L.; Zhuiykov, S. Atomic layer deposition-developed two-dimensional  $\alpha$ -MoO<sub>3</sub> windows excellent hydrogen peroxide electrochemical sensing capabilities. *Sens. Actuators B Chem.* **2018**, *262*, 334–344. [[CrossRef](#)]
31. Li, W.; Ou, Q.; Wang, X.; Xing, K.; Tesfamichael, T.; Motta, N.; Qi, D.-C. Large-sized  $\alpha$ -MoO<sub>3</sub> layered single crystals for superior NO<sub>2</sub> gas sensing. *Appl. Surf. Sci.* **2022**, *586*, 152793. [[CrossRef](#)]

32. Mei, J.; Liao, T.; Sun, Z. 2D/2D Heterostructures: Rational Design for Advanced Batteries and Electrocatalysis. *Energy Environ. Mater.* **2021**, *5*, 115–132. [[CrossRef](#)]
33. Bag, A.; Lee, N.-E. Gas sensing with heterostructures based on two-dimensional nanostructured materials: A review. *J. Mater. Chem. C* **2019**, *7*, 13367–13383. [[CrossRef](#)]
34. Guo, S.; Li, X.; Ren, X.; Yang, L.; Zhu, J.; Wei, B. Optical and Electrical Enhancement of Hydrogen Evolution by MoS<sub>2</sub>@MoO<sub>3</sub> Core-Shell Nanowires with Designed Tunable Plasmon Resonance. *Adv. Funct. Mater.* **2018**, *28*, 1802567. [[CrossRef](#)]
35. Hou, X.; Mensah, A.; Zhao, M.; Cai, Y.; Wei, Q. Facile controlled synthesis of monodispersed MoO<sub>3</sub>-MoS<sub>2</sub> hybrid nanospheres for efficient hydrogen evolution reaction. *Appl. Surf. Sci.* **2020**, *529*, 147115. [[CrossRef](#)]
36. Chen, Z.; Cummins, D.; Reinecke, B.N.; Clark, E.; Sunkara, M.K.; Jaramillo, T.F. Core-shell MoO<sub>3</sub>-MoS<sub>2</sub> Nanowires for Hydrogen Evolution: A Functional Design for Electrocatalytic Materials. *Nano Lett.* **2011**, *11*, 4168–4175. [[CrossRef](#)]
37. Zhao, S.; Zha, Z.; Liu, X.; Tian, H.; Wu, Z.; Li, W.; Sun, L.-B.; Liu, B.; Chen, Z. Core-Sheath Structured MoO<sub>3</sub>@MoS<sub>2</sub> Composite for High-Performance Lithium-Ion Battery Anodes. *Energy Fuels* **2020**, *34*, 11498–11507. [[CrossRef](#)]
38. Singh, S.; Guleria, A.; Singh, N.; Sharma, S. Highly responsive room-temperature ammonia sensing properties of MoS<sub>2</sub>/MoO<sub>3</sub> nano-composite. *Mater. Today Proc.* **2021**, *46*, 10732–10735. [[CrossRef](#)]
39. Li, J.; Xu, X.; Huang, B.; Lou, Z.; Li, B. Light-Induced In Situ Formation of a Nonmetallic Plasmonic MoS<sub>2</sub>/MoO<sub>3-x</sub> Heterostructure with Efficient Charge Transfer for CO<sub>2</sub> Reduction and SERS Detection. *ACS Appl. Mater. Interfaces* **2021**, *13*, 10047–10053. [[CrossRef](#)]
40. Pondick, J.V.; Woods, J.M.; Xing, J.; Zhou, Y.; Cha, J.J. Stepwise Sulfurization from MoO<sub>3</sub> to MoS<sub>2</sub> via Chemical Vapor Deposition. *ACS Appl. Nano Mater.* **2018**, *1*, 5655–5661. [[CrossRef](#)]
41. Heo, S.N.; Ishiguro, Y.; Hayakawa, R.; Chikyow, T.; Wakayama, Y. Perspective: Highly ordered MoS<sub>2</sub> thin films grown by multi-step chemical vapor deposition process. *APL Mater.* **2016**, *4*, 030901. [[CrossRef](#)]
42. Guo, Y.; Kang, L.; Song, P.; Zeng, Q.; Tang, B.; Yang, J.; Wu, Y.; Tian, D.; Xu, M.; Zhao, W.; et al. MoO<sub>3</sub>-MoS<sub>2</sub> vertical heterostructures synthesized via one-step CVD process for optoelectronics 2D. *Materials* **2021**, *8*, 035036. [[CrossRef](#)]
43. Weber, T.; Muijsers, J.C.; van Wolput, J.H.M.C.; Verhagen, C.P.J.; Niemantsverdriet, J.W. Basic reaction steps in the sulfidation of crystalline MoO<sub>3</sub> to MoS<sub>2</sub>, as studied by X-ray photoelectron and infrared emission spectroscopy. *J. Phys. Chem.* **1996**, *100*, 14144. [[CrossRef](#)]
44. Kumar, R.; Goel, N.; Mishra, M.; Gupta, G.; Fanetti, M.; Valant, M.; Kumar, M. Growth of MoS<sub>2</sub>-MoO<sub>3</sub> Hybrid Microflowers via Controlled Vapor Transport Process for Efficient Gas Sensing at Room Temperature. *Adv. Mater. Interfaces* **2018**, *5*, 1800071. [[CrossRef](#)]
45. Mohammadbeigi, M.; Jamilpanah, L.; Rahmati, B.; Mohseni, S.M. Sulfurization of planar MoO<sub>3</sub> optical crystals: Enhanced Raman response and surface porosity. *Mater. Res. Bull.* **2019**, *118*, 110527. [[CrossRef](#)]
46. Liu, H.; Lin, M.; Guo, S. Morphological and structural evolutions of  $\alpha$ -MoO<sub>3</sub> single crystal belts towards MoS<sub>2</sub>/MoO<sub>2</sub> heterostructures upon post-growth thermal vapor sulfurization. *Appl. Surf. Sci.* **2021**, *536*, 147956. [[CrossRef](#)]
47. Joya, M.R.; Alfonso, J.E.; Moreno, L.C. Photoluminescence and Raman studies of alpha-MoO<sub>3</sub> doped with erbium and neodymium. *Curr. Sci.* **2019**, *116*, 1690–1695. [[CrossRef](#)]
48. Diaz-Droguett, D.E.; El Far, R.; Fuenzalida, V.M.; Cabrera, A.L. In situ-Raman studies on thermally induced structural changes of porous MoO<sub>3</sub> prepared in vapor phase under He and H<sub>2</sub>. *Mater. Chem. Phys.* **2012**, *134*, 631–638. [[CrossRef](#)]
49. Camacho-López, M.A.; Escobar-Alarcón, L.; Picquart, M.; Arroyo, R.; Córdoba, G.; Haro-Poniatowski, E. Micro-Raman study of the m-MoO<sub>2</sub> to  $\alpha$ -MoO<sub>3</sub> transformation induced by cw-laser irradiation. *Opt. Mater.* **2011**, *33*, 480–484. [[CrossRef](#)]
50. Silveira, J.V.; Batista, J.A.; Saraiva, G.D.; Mendes Filho, J.; Souza Filho, A.G.; Hu, S.; Wang, X. Temperature dependent behavior of single walled MoO<sub>3</sub> nanotubes: A Raman spectroscopy study. *Vib. Spectrosc.* **2010**, *54*, 179–183. [[CrossRef](#)]
51. Singh, S.; Deb, J.; Sarkar, U.; Sharma, S. MoS<sub>2</sub>/MoO<sub>3</sub> Nanocomposite for Selective NH<sub>3</sub> Detection in a Humid Environment. *ACS Sustain. Chem. Eng.* **2021**, *9*, 7328–7340. [[CrossRef](#)]
52. Windom, B.C.; Sawyer, W.G.; Hahn, D.W. A Raman Spectroscopic Study of MoS<sub>2</sub> and MoO<sub>3</sub>: Applications to Tribological Systems. *Tribol. Lett.* **2011**, *42*, 301–310. [[CrossRef](#)]
53. Bera, A.; Sood, A.K. Insights into Vibrational and Electronic Properties of MoS<sub>2</sub> Using Raman, Photoluminescence, and Transport Studies. In *MoS<sub>2</sub>: Materials, Physics, and Devices*; Wang, Z.M., Ed.; Springer International Publishing: Cham, Switzerland, 2014; pp. 155–215.
54. Wang, D.; Li, J.-N.; Zhou, Y.; Xu, D.-H.; Xiong, X.; Peng, R.-W.; Wang, M. Van der Waals epitaxy of ultrathin  $\alpha$ -MoO<sub>3</sub> sheets on mica substrate with single-unit-cell thickness. *Appl. Phys. Lett.* **2016**, *108*, 053107. [[CrossRef](#)]
55. Song, L.X.; Xia, J.; Dang, Z.; Yang, J.; Wang, L.B.; Chen, J. Formation, structure and physical properties of a series of  $\alpha$ -MoO<sub>3</sub> nanocrystals: From 3D to 1D and 2D. *Cryst. Eng. Comm.* **2012**, *14*, 2675–2682. [[CrossRef](#)]
56. Song, S.; Wang, J.; Peng, T.; Fu, W.; Zan, L. MoS<sub>2</sub>-MoO<sub>3-x</sub> hybrid cocatalyst for effectively enhanced H<sub>2</sub> production photoactivity of AgIn<sub>5</sub>S<sub>8</sub> nano-octahedrons. *Appl. Catal. B Environ.* **2018**, *228*, 39–46. [[CrossRef](#)]
57. Szoszkiewicz, R.; Rogala, M.; Dąbrowski, P. Surface-Bound and Volatile Mo Oxides Produced During Oxidation of Single MoS<sub>2</sub> Crystals in Air and High Relative Humidity. *Materials* **2020**, *13*, 3067. [[CrossRef](#)] [[PubMed](#)]
58. Hao, S.; Yang, B.; Gao, Y. Chemical vapor deposition growth and characterization of drop-like MoS<sub>2</sub>/MoO<sub>2</sub> granular films. *Phys. Status Solidi* **2017**, *254*, 1600245. [[CrossRef](#)]

59. Wang, L.; Ji, X.; Wang, T.; Zhang, Q. Novel Red Emission from MoO<sub>3</sub>/MoS<sub>2</sub>-MoO<sub>2</sub>-MoO<sub>3</sub> Core-Shell Belt Surface. *ACS Appl. Mater. Interfaces* **2018**, *10*, 36297–36303. [[CrossRef](#)]
60. Yoon, A.; Kim, J.H.; Yoon, J.; Lee, Y.; Lee, Z. van der Waals Epitaxial Formation of Atomic Layered  $\alpha$ -MoO<sub>3</sub> on MoS<sub>2</sub> by Oxidation. *ACS Appl. Mater. Interfaces* **2020**, *12*, 22029–22036. [[CrossRef](#)]
61. Kibsgaard, J.; Chen, Z.; Reinecke, B.N.; Jaramillo, T.F. Engineering the surface structure of MoS<sub>2</sub> to preferentially expose active edge sites for electrocatalysis. *Nat. Mater.* **2012**, *11*, 963–969. [[CrossRef](#)]
62. Brown, N.M.D.; Cui, N.; McKinley, A. An XPS study of the surface modification of natural MoS<sub>2</sub> following treatment in an RF-oxygen plasma. *Appl. Surf. Sci.* **1998**, *134*, 11–21. [[CrossRef](#)]
63. Ou, J.Z.; Ge, W.; Carey, B.; Daeneke, T.; Rotbart, A.; Shan, W.; Wang, Y.; Fu, Z.; Chrimes, A.F.; Wlodarski, W.; et al. Physisorption-Based Charge Transfer in Two-Dimensional SnS<sub>2</sub> for Selective and Reversible NO<sub>2</sub> Gas Sensing. *ACS Nano* **2015**, *9*, 10313–10323. [[CrossRef](#)] [[PubMed](#)]
64. Zhou, X.Y.; Wang, R.; Meng, L.J.; Xu, X.Y.; Hu, J.G.; Pan, J. Achieving half-metallicity in zigzag MoS<sub>2</sub> nanoribbon with a sulfur vacancy by edge passivation. *J. Phys. D Appl. Phys.* **2018**, *51*, 265005. [[CrossRef](#)]
65. Lee, D.J.; Lee, Y.; Kwon, Y.H.; Choi, S.H.; Yang, W.; Kim, D.Y.; Lee, S. Room-Temperature Ferromagnetic Ultrathin  $\alpha$ -MoO<sub>3</sub>:Te Nanoflakes. *ACS Nano* **2019**, *13*, 8717–8724. [[CrossRef](#)] [[PubMed](#)]
66. Brinkman, A.; Huijben, M.; van Zalk, M.; Huijben, J.; Zeitler, U.; Maan, J.C.; van der Wiel, W.G.; Rijnders, G.; Blank, D.H.A.; Hilgenkamp, H. Magnetic effects at the interface between non-magnetic oxides. *Nat. Mater.* **2007**, *6*, 493–496. [[CrossRef](#)]
67. Shidpour, R.; Manteghian, M. A density functional study of strong local magnetism creation on MoS<sub>2</sub> nanoribbon by sulfur vacancy. *Nanoscale* **2010**, *2*, 1429–1435. [[CrossRef](#)]
68. Rusydi, A.; Dhar, S.; Barman, A.R.; Ariando, n.; Qi, D.C.; Motapothula, M.; Yi, J.B.; Santoso, I.; Feng, Y.P.; Yang, K.; et al. Cationic-vacancy-induced room-temperature ferromagnetism in transparent, conducting anatase Ti<sub>1-x</sub>Ta<sub>x</sub>O<sub>2</sub> (x~0.05) thin films. *Philos. Trans. R. Soc. A Math. Phys. Eng. Sci.* **2012**, *370*, 4927–4943. [[CrossRef](#)]
69. Mao, Y.; Li, W.; Sun, X.; Ma, Y.; Xia, J.; Zhao, Y.; Lu, X.; Gan, J.; Liu, Z.; Chen, J.; et al. Room-temperature ferromagnetism in hierarchically branched MoO<sub>3</sub> nanostructures. *Crystengcomm* **2012**, *14*, 1419–1424. [[CrossRef](#)]
70. Botello-Méndez, A.R.; López-Urías, F.; Terrones, M.; Terrones, H. Metallic and ferromagnetic edges in molybdenum disulfide nanoribbons. *Nanotechnology* **2009**, *20*, 325703. [[CrossRef](#)]
71. Li, Y.; Song, Z.; Li, Y.; Li, S.; Wang, H.; Song, B.; Gao, B.; Du, X. Synthesis of Mo<sub>4</sub>O<sub>11</sub>@MoO<sub>3</sub> nanobelts and their improved sensing performance to NO<sub>2</sub> gas. *Mater. Res. Express* **2019**, *6*, 055041. [[CrossRef](#)]
72. Analytical Methods, C. Recommendations for the definition, estimation and use of the detection limit. *Analyst* **1987**, *112*, 199–204. [[CrossRef](#)]
73. Shafiei, M.; Bradford, J.; Khan, H.; Piloto, C.; Wlodarski, W.; Li, Y.; Motta, N. Low-operating temperature NO<sub>2</sub> gas sensors based on hybrid two-dimensional SnS<sub>2</sub>-reduced graphene oxide. *Appl. Surf. Sci.* **2018**, *462*, 330–336. [[CrossRef](#)]
74. Acharyya, D.; Huang, K.Y.; Chattopadhyay, P.P.; Ho, M.S.; Fecht, H.J.; Bhattacharyya, P. Hybrid 3D structures of ZnO nanoflowers and PdO nanoparticles as a highly selective methanol sensor. *Analyst* **2016**, *141*, 2977–2989. [[CrossRef](#)] [[PubMed](#)]
75. Russell, S.A.O.; Cao, L.; Qi, D.C.; Tallaire, A.; Crawford, K.G.; Wee, A.T.S.; Moran, D.A.J. Surface transfer doping of diamond by MoO<sub>3</sub>: A combined spectroscopic and Hall measurement study. *Appl. Phys. Lett.* **2013**, *103*, 202112. [[CrossRef](#)]
76. Li, S.; Ma, Y.; Ouedraogo, N.A.N.; Liu, F.; You, C.; Deng, W.; Zhang, Y. p-/n-Type modulation of 2D transition metal dichalcogenides for electronic and optoelectronic devices. *Nano Res.* **2022**, *15*, 123–144. [[CrossRef](#)]
77. Miller, D.R.; Akbar, S.A.; Morris, P.A. Nanoscale metal oxide-based heterojunctions for gas sensing: A review. *Sens. Actuator B-Chem.* **2014**, *204*, 250–272. [[CrossRef](#)]
78. Xing, K.; Xiang, Y.; Jiang, M.; Creedon, D.L.; Akhgar, G.; Yianni, S.A.; Xiao, H.; Ley, L.; Stacey, A.; McCallum, J.C.; et al. MoO<sub>3</sub> induces p-type surface conductivity by surface transfer doping in diamond. *Appl. Surf. Sci.* **2020**, *509*, 144890. [[CrossRef](#)]
79. Xing, K.; Li, W.; Della Gaspera, E.; van Embden, J.; Zhang, L.; Yianni, S.A.; Creedon, D.L.; Wang, T.; McCallum, J.C.; Wang, L.; et al. Surface transfer doping of diamond using solution-processed molybdenum trioxide. *Carbon* **2021**, *175*, 20–26. [[CrossRef](#)]
80. Keyshar, K.; Berg, M.; Zhang, X.; Vajtai, R.; Gupta, G.; Chan, C.K.; Beechem, T.E.; Ajayan, P.M.; Mohite, A.D.; Ohta, T. Experimental Determination of the Ionization Energies of MoSe<sub>2</sub>, WS<sub>2</sub>, and MoS<sub>2</sub> on SiO<sub>2</sub> Using Photoemission Electron Microscopy. *ACS Nano* **2017**, *11*, 8223–8230. [[CrossRef](#)]
81. McDonnell, S.; Azcatl, A.; Addou, R.; Gong, C.; Battaglia, C.; Chuang, S.; Cho, K.; Javey, A.; Wallace, R.M. Hole Contacts on Transition Metal Dichalcogenides: Interface Chemistry and Band Alignments. *ACS Nano* **2014**, *8*, 6265–6272. [[CrossRef](#)]
82. Pal, S.; Mukherjee, S.; Nand, M.; Srivastava, H.; Mukherjee, C.; Jha, S.N.; Ray, S.K. Si compatible MoO<sub>3</sub>/MoS<sub>2</sub> core-shell quantum dots for wavelength tunable photodetection in wide visible range. *Appl. Surf. Sci.* **2020**, *502*, 144196. [[CrossRef](#)]
83. Hung, C.M.; Vuong, V.A.; Duy, N.V.; An, D.V.; Hieu, N.V.; Kashif, M.; Hoa, N.D. Controlled Growth of Vertically Oriented Trilayer MoS<sub>2</sub> Nanoflakes for Room-Temperature NO<sub>2</sub> Gas Sensor Applications. *Phys. Status Solidi* **2020**, *217*, 2000004. [[CrossRef](#)]
84. Yan, W.; Yan, W.; Chen, T.; Xu, J.; Tian, Q.; Ho, D. Size-Tunable Flowerlike MoS<sub>2</sub> Nanospheres Combined with Laser-Induced Graphene Electrodes for NO<sub>2</sub> Sensing. *ACS Appl. Nano Mater.* **2020**, *3*, 2545–2553. [[CrossRef](#)]
85. Thang, N.T.; Hong, L.T.; Thoan, N.H.; Hung, C.M.; Van Duy, N.; Van Hieu, N.; Hoa, N.D. Controlled synthesis of ultrathin MoS<sub>2</sub> nanoflowers for highly enhanced NO<sub>2</sub> sensing at room temperature. *RSC Adv.* **2020**, *10*, 12759–12771. [[CrossRef](#)]

86. Kwon, H.I. Low-temperature-operated sensitive NO<sub>2</sub> gas sensors based on p-type SnO thin-film and thin-film transistors. In Proceedings of the 2020 27th International Workshop on Active-Matrix Flatpanel Displays and Devices (AM-FPD), Kyoto, Japan, 1–4 September 2020; pp. 55–58.
87. Yu, L.; Guo, F.; Liu, S.; Qi, J.; Yin, M.; Yang, B.; Liu, Z.; Fan, X.H. Hierarchical 3D flower-like MoS<sub>2</sub> spheres: Post-thermal treatment in vacuum and their NO<sub>2</sub> sensing properties. *Mater. Lett.* **2016**, *183*, 122–126. [[CrossRef](#)]
88. Zhu, Q.; Wang, H.; Yang, J.; Xie, C.; Zeng, D.; Zhao, N. Red Phosphorus: An Elementary Semiconductor for Room-Temperature NO<sub>2</sub> Gas Sensing. *ACS Sens.* **2018**, *3*, 2629–2636. [[CrossRef](#)]
89. Yamada, Y.; Ogita, M. Transient response of resistive-type NO<sub>2</sub> sensor on temperature change. *Sens. Actuators B Chem.* **2003**, *93*, 546–551. [[CrossRef](#)]
90. Yang, L.; Xie, C.; Zhang, G.; Zhao, J.; Yu, X.; Zeng, D.; Zhang, S. Enhanced response to NO<sub>2</sub> with CuO/ZnO laminated heterostructured configuration. *Sens. Actuators B Chem.* **2014**, *195*, 500–508. [[CrossRef](#)]